DC electrical conductivity measurements of warm dense matter using ultrafast THz radiation

Ofori-Okai, B. K., Descamps, A., McBride, E. E., Mo, M. Z., Weinmann, A., Seipp, L. E., Ali, S. J., Chen, Z., Fletcher, L. B., & Glenzer, S. H. (2024). DC electrical conductivity measurements of warm dense matter using ultrafast THz radiation. *Physics of Plasmas*, *31*(4), Article 042711. https://doi.org/10.1063/5.0193854

DC electrical conductivity measurements of warm dense matter using ultrafast THz radiation ⊞

B. K. Ofori-Okai ✉ iD ; A. Descamps iD ; E. E. McBride iD ; M. Z. Mo iD ; A. Weinmann iD ; L. E. Seipp;
S. J. Ali iD ; Z. Chen; L. B. Fletcher iD ; S. H. Glenzer iD

Check for updates

View Online   Export Citation

DC electrical conductivity measurements of warm dense matter using ultrafast THz radiation EP

View Online   Export Citation   CrossMark

B. K. Ofori-Okai,[1,2,a)] (iD) A. Descamps,[1,3] (iD) E. E. McBride,[1,3] (iD) M. Z. Mo,[1] (iD) A. Weinmann,[1,4] (iD) L. E. Seipp,[1,4] S. J. Ali,[5] (iD) Z. Chen,[1] L. B. Fletcher,[1] (iD) and S. H. Glenzer[1,b)] (iD)

AFFILIATIONS

[1]SLAC National Accelerator Laboratory, 2575 Sand Hill Road, Menlo Park, California 94025, USA
[2]PULSE Institute, SLAC National Accelerator Laboratory, 2575 Sand Hill Road, Menlo Park, California 94025, USA
[3]School of Mathematics and Physics, Queen's University Belfast, University Rd, Belfast BT7 1NN, United Kingdom
[4]Universität der Bundeswehr München, Werner-Heisenberg-Weg 39, 85579 Neubiberg, Germany
[5]Lawrence Livermore National Laboratory, 7000 East Avenue, Livermore, California 94550, USA

Note: This paper is part of the Special Topic: Charged-Particle Transport in High Energy Density Plasmas.
Note: This paper is part of the Special Topic: Papers from the 62nd Annual Meeting of the APS Division of Plasma Physics.
[a)]Author to whom correspondence should be addressed: benofori@SLAC.stanford.edu
[b)]Electronic mail: glenzer@SLAC.stanford.edu

ABSTRACT

We describe measurements of the DC electrical conductivity of warm dense matter using ultrafast terahertz (THz) pulses. THz fields are sufficiently slowly varying that they behave like DC fields on the timescale of electron–electron and electron–ion interactions and hence probe DC-like responses. Using a novel single-shot electro-optic sampling technique, the electrical conductivity of the laser-generated warm dense matter was determined with <1 ps temporal resolution. We present the details of the single-shot THz detection methodology as well as considerations for warm dense matter experiments. We, then, provide proof-of-concept studies on aluminum driven to the warm dense matter regime through isochoric heating and shock compression. Our results indicate a decrease in the conductivity when driven to warm dense matter conditions and provide a platform for future warm dense matter studies.

I. INTRODUCTION

The zero-frequency (DC or electrical) conductivity is a critical parameter for modeling processes relevant for high energy density science, including predicting the growth of Rayleigh–Taylor instabilities in inertial confinement fusion (ICF)[1,2] or for modeling magnetic fields produced by planetary dynamos.[3,4] The challenge in predicting electrical conductivities for these situations is that the relevant conditions lie in the warm dense matter (WDM) regime, where the material temperature is on the order of ~ 0.1–$10\,\mathrm{eV}$ and the material density is ~ 0.1–$10\times$ that of a solid.[5–7] At these conditions, the thermal energy is comparable to the electron energy at the Fermi level, and this, combined with the strong Coulomb coupling, results in significant deviation from ideal plasma behavior. As such, conventional conductivity models, such as those of Spitzer,[8] Kubo–Greenwood,[9] Ziman,[10] or Lee–More[11] breakdown in the WDM regime. Recently, density functional theory calculations have been used to predict the conductivity of

WDM based on the Kubo–Greenwood formalism;[12–18] however, experimental data are needed to test and improve theory.

With the development of high-intensity and high-energy lasers, WDM can be generated for a short time (few picoseconds to nanoseconds) in a laboratory before irreversibly changing into a plasma.[19–26] Given that laboratory WDM exists transiently, single shot diagnostics with temporal resolution high enough to capture short-lived states are vital for interrogating WDM. The high-frequency (AC or optical) conductivity at visible frequencies can be determined by measuring the optical reflectivity using nanosecond pulses and a time-resolving detector[22,24,27,28] and using ultrafast laser pulses with a duration of a few to hundreds of femtoseconds.[20,29–31] In principle, the optical conductivity can be used to determine the electrical conductivity. However, this requires knowing the frequency dependence of the dielectric function from high-to-low frequency which is *a priori* unknown. Another approach is to use inelastic x-ray scattering (x-ray Thomson scattering,

XRTS),[32] to extrapolate the conductivity from the plasmon response.[33,34] However, these extrapolations are highly model dependent.

A promising method for measuring the electrical conductivity of WDM is terahertz time-domain spectroscopy (THz-TDS).[35–37] Unlike visible and near-infrared frequency pulses, the THz electric field oscillates slowly when compared with electron scattering time, τ. In the context of the Drude model, where the frequency dependent conductivity, $\tilde{\sigma}(\omega)$, is given by

$$\tilde{\sigma}(\omega) = \frac{\sigma_0}{1 - i\omega\tau} = \frac{n_e q^2 \tau / m_e}{1 - i\omega\tau}, \tag{1}$$

where σ_0 is the DC conductivity, n_e is the free electron density, q is the charge on an electron, and m_e is the free electron mass, $\tau \sim 10$ fs in typical metals,[38] possibly shorter in WDM.[30] As such, in the range $\omega/2\pi \sim 1$ THz, $\omega\tau \ll 1$ and consequently $\tilde{\sigma}(\omega) \to \sigma_0$. This indicates that THz frequency radiation more appropriately probes the DC conductivity.

In conventional THz-TDS, the electric field of a coherent broadband THz frequency pulse is measured in the time-domain, $E(t)$, and the complex-valued spectrum, $\tilde{E}(\omega)$, is obtained by a numerical Fourier transform.[39–41] Coherent THz pulses can be produced by optical rectification in nonlinear crystals[40,42,43] or by free-electron lasers (FELs).[44–48] By measuring changes in the spectrum of a THz pulse that has interacted with a sample, the complex-valued dielectric function, $\tilde{\varepsilon}(\omega)$, can be obtained, and this is related to the complex conductivity. Conveniently, this is a noninvasive method, meaning that no leads or wires need to physically touch the sample. THz-TDS has been used to characterize materials in condensed phases and integrated into pump-probe geometries to study the evolution of conductivity following photoexcitation.[49–52] The most commonly used approaches for THz time-domain detection require hundreds to thousands of laser pulses, however, and are implemented using laser systems that operate at kHz to MHz repetition rates. This is impractical for WDM experiments where the sample is destroyed after a single laser exposure.

In order to implement THz-TDS for WDM studies, single-shot techniques for capturing the THz time-domain waveform are required. The development of single-shot schemes has been an active area of research. Recently, a single-shot approach has emerged using an echelon-based scheme that meets the requirements for THz measurements.[53] The combination of bright THz sources and detection with the sufficiently high signal-to-noise of this method have opened the door for studies of irreversible processes, as has been demonstrated.[54–57]

In this paper, we discuss the implementation of THz spectroscopy for studies on WDM. Following this Introduction, Sec. II discusses electro-optic (EO) sampling, with a review of the convectional approach used for studies of reversible phenomena, including the details of the non-linear optics approach to conventional THz detection. Section III discusses single shot detection with echelons, with a focus on signal-to-noise reduction and considerations for WDM experiments. Section IV then presents applications of THz experiments on two cases of interest to WDM studies: isochoric heating of the thin film and measurements of the laser compressed matter. Finally, we conclude with an overall summary, suggesting areas for improvement and future directions.

II. PRINCIPLES OF ELECTRO-OPTIC SAMPLING

One of the most commonly used methods for free-space THz detection is electro-optic (EO) sampling.[39,40,58] A schematic of an EO sampling setup is shown in Fig. 1. In conventional EO sampling, the THz pulse propagates co-linearly with a linearly polarized femtosecond laser pulse, the sampling pulse, through a nonlinear optical medium, hereafter referred to as the EO sampling crystal or EO crystal; in the presented case, it is a (1 1 0)-cut of either zinc telluride (ZnTe) or gallium phosphide (GaP). The THz electric field changes the optical properties of the EO crystal, and these changes are encoded as a polarization change in the sampling pulse. By measuring the polarization change, the THz electric field can be extracted.

A. Theoretical background

Detailed treatments of EO sampling have been worked out previously.[59–61] In this section, we only describe the key results. In the Appendix, we provide a more thorough derivation of the starting equations from nonlinear optics. ZnTe or GaP are initially optically isotropic, with refractive indices $n_x = n_y = n_z = n_0$. When the THz field is present, it changes the refractive indices of the EO crystal via the Pockels effect, a linear change of a material's refractive index in the presence of a static electric field,[62–64] and makes the EO crystal transiently anisotropic. For ZnTe-(1 1 0) or GaP-(1 1 0), the electric field of the THz pulse changes the refractive indices according to

$$\Delta n_x = -\frac{1}{2} r_{41} n_0^3 E_{THz} \cos(\alpha), \tag{2a}$$

$$\Delta n_y = \frac{1}{2} r_{41} n_0^3 E_{THz} \left[\cos(\alpha) \sin^2(\psi) + \cos(\alpha + 2\psi) \right], \tag{2b}$$

$$\Delta n_z = \frac{1}{2} r_{41} n_0^3 E_{THz} \left[\cos(\alpha) \cos^2(\psi) - \cos(\alpha + 2\psi) \right]. \tag{2c}$$

Here, E_{THz} is the THz electric field, α is the polarization angle of the THz field with respect to the [0 0 1] axis, r_{41} is the relevant nonlinear
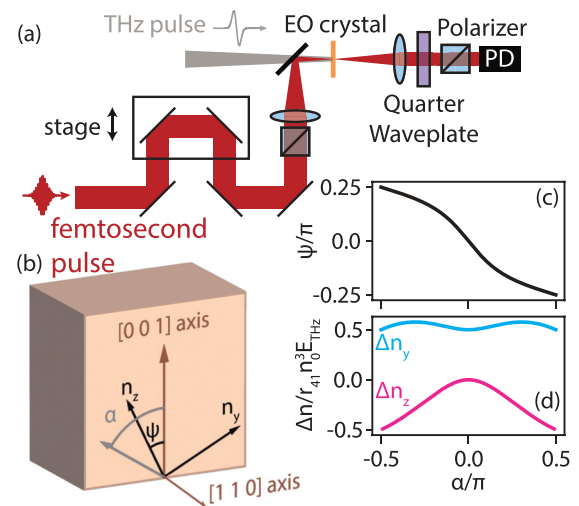

FIG. 1. (a) Schematic of a setup for EO sampling. (b) Schematic of the EO crystal with the relevant axes and angles labeled. The gray arrow represents the THz polarization, which makes an angle α with the [0 0 1] axis of the EO crystal. Plots of (c) ψ and (d) change in the refractive indices Δn_y and Δn_z for different values of α.

tensor element, and ψ is the angle between the [0 0 1] axis and the fast optical axis of the crystal, n_z. The angle between the fast and slow axes is always 90°. ψ is related to α by

$$\psi = \frac{1}{2}\arctan(-2\tan(\alpha)). \qquad (3)$$

In EO sampling, the THz and sampling pulses propagate along the [1 1 0] axis, parallel to n_x. Therefore, the relevant induced anisotropy, or birefringence, is between the n_y and n_z axes. For the sampling pulse, this birefringence causes a change in the optical phase of the components of the sampling pulse projected along n_y and n_z. The optical phase difference accumulated when propagating through a thickness ℓ of the EO crystal is

$$\Delta\phi = \frac{2\pi\ell}{\lambda}(\Delta n_y - \Delta n_z), \qquad (4)$$

where λ is the center wavelength of the sampling pulse. Using Eqs. (2b), (2c), and (3), one can determine that $\Delta\phi$ is maximized for $\alpha = \pm\pi/2$. This means that if the THz field is horizontally polarized in the lab frame, the [0 0 1] axis of the EO crystal should be oriented vertically. The fast and slow axes of the EO crystal are then at $\pm 45°$ relative to vertical (and horizontal). The maximum phase change will then occur if the polarization of the sampling pulse is either horizontal or vertical.[60]

The phase change in the sampling pulse manifests as a modulation of the polarization, making the initially linear polarization of the pulse elliptical. The ellipticity is measured using a quarter wave plate, a polarizer oriented perpendicular to the initial polarization, and a photodiode. The action of the waveplate and polarizer converts the polarization change into an intensity change, which is measured on the photodiode. Using Jones calculus[63] for the configuration described above, one finds that when the fast axis of the quarter wave plate is set 45° relative to the axes of the polarizer, the measured intensity on the photodiode, I, is

$$I = I_0[1 + \sin(\Delta\phi)] = I_0\left[1 + \sin\left(\frac{2\pi\ell}{\lambda}r_{41}n_0^3 E_{\mathrm{THz}}\right)\right], \qquad (5)$$

where I_0 is the intensity of the sampling pulse when no THz field is present. The full THz time-domain waveform, $E_{\mathrm{THz}}(t)$, is determined by measuring I for different timing between the sampling pulse and the THz pulse, for example, by using a mechanical stage, shown in Fig. 1, to change the path length traveled by the sampling pulse.

B. Methods for noise reduction

From Eq. (5), optimizing the signal can be accomplished through ℓ, r_{41}, n_0. The choice of material for the EO crystal will influence all of these parameters; R_{41} and n_0 are material specific. Typical values for n_0 are ~ 2–3 (see Ref. 65), while r_{41} can vary by up to an order of magnitude, making this term dominate. The maximum thickness, ℓ_M, is dependent on the velocity mismatch between the pulses. We can determine ℓ_M as

$$\ell_M = \frac{\pi c_0}{\omega_{\mathrm{THz}}|n_g - n_{\mathrm{THz}}|}. \qquad (6)$$

Here, ω_{THz} is the THz angular frequency, n_g is the group refractive index of the sampling pulse, n_{THz} is the THz refractive index at ω_{THz},

and ℓ_M, thus, corresponds to the distance over which the THz and sampling pulses will slip by a half-period of the THz cycle. Finally, the material will also limit the detectable bandwidth due to absorption of THz radiation. ZnTe is often chosen for THz pulses with spectral bandwidth less than 2.5 THz, as $\ell_M \sim 2.5$ mm and r_{41} is large. While GaP has a much lower r_{41} and $\ell_M \sim 0.2$ mm, it is weakly absorbing below 7 THz, and so it is also used.

While measuring I alone is, in principle, sufficient to extract E_{THz}, only measuring I limits of the sensitivity of the EO sampling. For laser systems with slow stochastic drifts in laser energy, this can produce modulations that are indistinguishable from those induced by the THz signal. Similarly, large shot-to-shot fluctuations lead to significant noise. These effects can be mitigated and the sensitivity of EO sampling can be greatly improved by normalizing the intensity of the sampling pulse and using balanced detection to improve the signal-to-noise ratio.

To normalize the intensity, a measurement of the sampling pulse without the THz field present is required. This yields I_0, which can be used to determine the corresponding relative intensity change in the sampling pulse, $\Delta I/I_0$,

$$\frac{I}{I_0} - 1 = \frac{\Delta I}{I_0} = \sin(\Delta\phi). \qquad (7)$$

Compared to measuring I alone, $\Delta I/I_0$ has the advantage that it can be used to determine $\Delta\phi$, which is a function of E_{THz}. One strategy to determine I_0 is by averaging measurements of the sampling pulse either long before or after the measurement with the THz pulse. This, however, only re-scales the data and does not compensate for slow drift. Instead, measuring I_0 as close in time as possible as I is measured reduces effects from the long-term drift in the laser energy.

In addition to intensity normalization, balanced detection can be implemented to correct for shot-to-shot fluctuations in the laser energy. In traditional balanced detection, the sampling pulse is split and bypasses the EO crystal, and I and I_0 are measured on separate photodetectors. However, for EO sampling, an advantage can be leveraged by using a polarizing beam splitter or a Wollaston prism to measure pulses with orthogonal polarizations. Compared to the signal described by Eq. (5), referred to as I^+, the intensity in the other polarization is $I^- = I_0^-[1 - \sin(\Delta\phi)]$. The signal $S(t)$ can then be constructed as

$$S(t) = \frac{\Delta I^+}{I_0^+}(t) - \frac{\Delta I^-}{I_0^-}(t) = 2\sin\left(\frac{2\pi\ell}{\lambda}r_{41}n_0^3 E_{\mathrm{THz}}(t)\right). \qquad (8)$$

This version of balanced detection has the advantage that the signal is doubled, while at the same time fluctuations in the sampling pulse between the measurements of $I^\pm$ and $I_0^\pm$ are subtracted out. This leads to a greater than $2\times$ increase in the signal-to-noise ratio (SNR). In some cases, a $10\times$ improvement can be obtained.[66]

III. ECHELON-BASED SINGLE-SHOT DETECTION

The main limitation of EO sampling for WDM studies is that multiple shots are required to measure the time-domain waveform. Often, a mechanical delay stage is moved to vary the arrival time of the sampling pulse relative to the THz pulses, and I and I_0 are measured at each relative delay. Consequently, measurements where the sample is irreversible changed or destroyed require more sophisticated detection methods. This has been one motivation for the development of

single-shot EO sampling techniques. Recent work by Teo et al.[53] investigated multiple different approaches and determined that the use of echelons was the most promising method for single-shot THz detection. In this context, an echelon is an optical element with multiple steps cut into a bulk material.[54,67]

A schematic of a reflective echelon is shown in Fig. 2(a). Unlike a grating, the steps of an echelon are larger than the wavelength of the sampling pulse. As such, each step of the echelon acts as a mirror and specularly reflects a different part of the beam. Additionally, each reflected part of the beam travels a slightly different distance, which results in a time delay, Δt, given by

$$\Delta t = \frac{2H}{c_0 \cos{(\theta_i)}}, \tag{9}$$

where H is the step height, c_0 is the speed of light, and θ_i is the angle of incidence of the beam with respect to the echelon step normal. For the data in this work, $H = 5.00 \pm 0.02\,\mu m$ and $\Delta t \approx 33\,fs$. The overall effect turns a single input pulse into a series of time-delayed pulses, thereby replacing the need to scan the mechanical stage. The total time

FIG. 2. (a) Schematic illustration of how the echelon used for single-shot EO sampling. (b) Raw images of echelon measured after passing through Wollaston prism. The two squares correspond to I^+ and I^-, as the THz pulse is present, leading to modulation of the intensity from left to right. (c) The result of normalizing the image in panel (b) with ones where the THz pulse is absent, yielding $\Delta I^+/I_0^+$ and $\Delta I^-/I_0^-$.

window was $N\Delta t = 15\,ps$, where $N = 500$ is the number of steps on the echelon. Using a lens, these pulses are focused into the EO sampling crystal and different segments of the THz pulse are encoded on different spatial locations of the sampling beam. The THz waveform is determined using the same polarization optics as described in Sec. II; however, a charge coupled device (CCD) or complementary metal oxide semiconductor (CMOS) camera replaces the photodiodes and the echelon must be imaged onto the camera.

Figure 2(b) shows an image collected when the THz pulse is overlapped with the sampling pulses in a 2 mm thick ZnTe crystal. The two squares correspond to the different polarization states produced by the Wollaston prism. Figure 2(c) shows the result of dividing the image in Fig. 2(b) by an image collected with the THz pulse is absent, highlighting where the THz field has changed the polarization of the sampling pulses. Here, time is mapped to the horizontal position of the echelon image as the steps of the echelon run along the vertical axis. The time axis is pre-calibrated by adjusting the arrival time of the THz pulse and sampling pulses using a mechanical stage. This calibration can be re-used provided the imaging system remains unchanged.
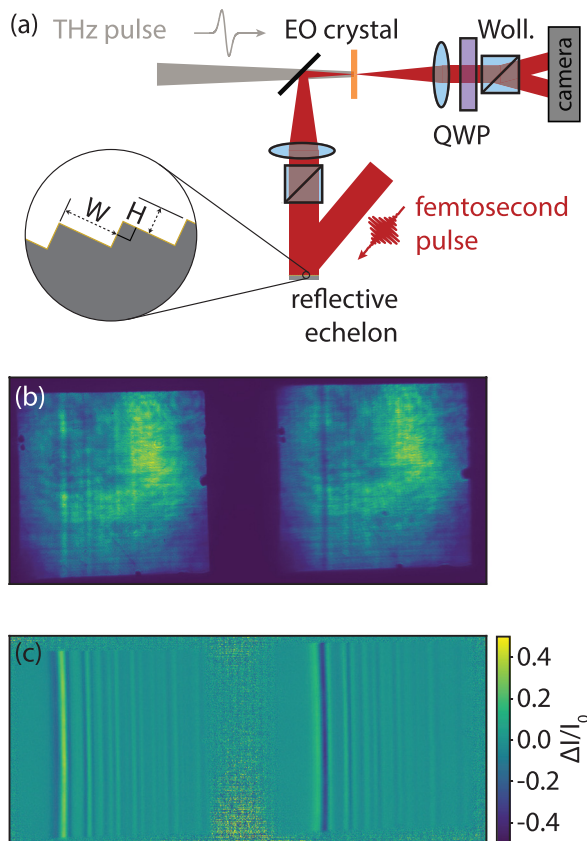
A. Signal extraction and effects of noise reduction

In the data, the modulation is uniform along the vertical axis, and so the THz waveform can be extracted by averaging along the vertical axis. Doing so for the raw images yields the waveforms shown in Figs. 3(a) and 3(b). The THz signal can be seen on top of a large slowly vary background, which arises due spatial inhomogeneities in the illumination of the echelon square. This is analogous to the effect of slow laser energy drift in scanning EO sampling. The difference in intensity was due to intentional misalignment of the quarter wave plate in that dataset to compensate for parasitic static birefringence of the ZnTe crystal used in these measurements. By comparison, Figs. 3(c) and 3(d) show the waveforms extracted from normalized images. After normalization, the background is flat, and the signals have opposite sign as expected from the Jones calculus analysis. Figure 3(e) shows the waveform obtained by balancing, demonstrating the doubling of the signal intensity.

One important advantage of both conventional and single-shot EO sampling are that they record the THz field, rather than the intensity. From the field, the amplitude and phase of the frequency-domain spectrum, $\tilde{E}(\omega) = A(\omega)\exp{[i\phi(\omega)]}$, can be determined through a numerical Fourier transform. This permits direct access to the real and imaginary parts of optical and material properties, such as the refractive index or the conductivity,[35] eliminating the need for full knowledge of the dielectric function which is a requirement for Kramers–Kronig analysis.

Figure 3(f) shows the THz amplitude spectrum. In this system, the maximum detected frequency slightly exceeds 2 THz. This is set by the details of the THz source, the type of detection crystal and its thickness, and the duration of the sampling pulses. For the data presented, the THz pulse was generated by optical rectification in a 2 mm thick ZnTe crystal. With this setup, we are able to record THz waveforms in a single shot with a SNR of >200:1. Additionally, the reproducibility of the system allows for averaging of multiple measurements to accurately investigate WDM.

B. Considerations for warm dense matter experiments

In the data in Fig. 3, the THz waveform begins with a pulse centered at 5 ps and has subsequent oscillations. These oscillations are due
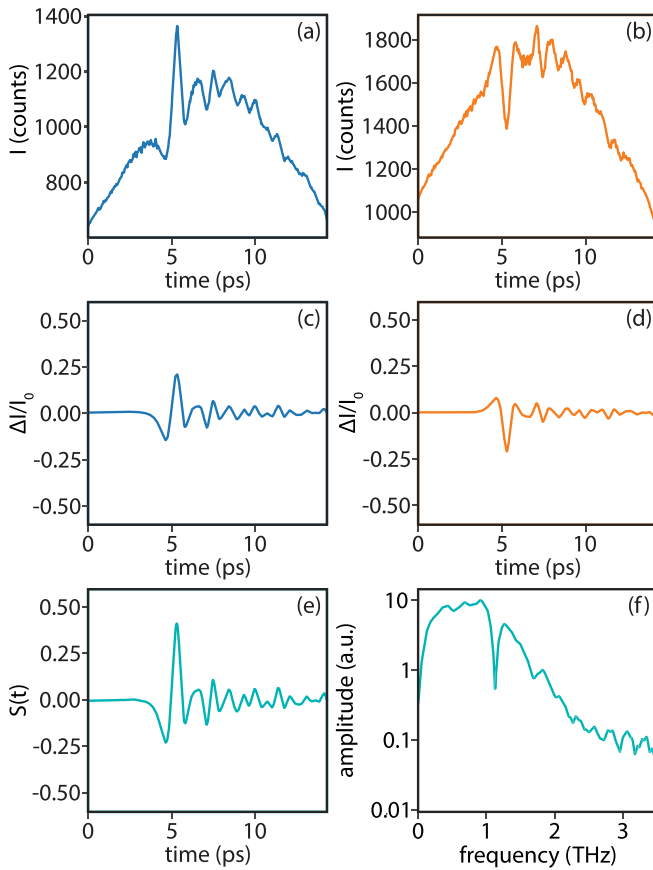
FIG. 3. (a) and (b) THz time-domain waveforms extracted from unnormalized images of different polarization states produced by the Wollaston prism. (c) and (d) Waveforms extracted from normalized images. (e) Balanced signal obtained by taking the difference between the waveforms. (f) Spectrum of THz pulse obtained by Fourier transformation of the time-domain waveform.

FIG. 4. (a) THz waveforms and (b) corresponding spectra for cases of different relative humidity within the experimental chamber. (c) THz waveforms and (d) spectra in the case that pinholes of various diameters are placed at the focal plane of an $f/1$ parabolic mirror. The effect of different frequencies focusing to different sizes reduces the signal amplitude and changes the spectrum.

to absorption of the THz field by ambient water vapor. Ambient water vapor absorbs THz radiation at well-defined frequencies due to resonant rotational modes and vibrational bands as well as broadband absorption.[68,69] This modifies $E(t)$ directly, and the oscillations cannot be observed without the THz pulse. The resonant absorption is also visible as dips in the frequency domain. These can be seen in in the teal curves in Figs. 4(a) and 4(b), where the relative humidity measured by an independent sensor was ~53%. These result in unwanted contributions and limit the sensitivity of the measurement, in particular, in the frequency domain where the regions of low signal have a lower dynamic range.

These effects can be removed by performing experiments in a vacuum chamber, as commonly done in WDM experiments, or in an enclosure flushed with an inert gas (e.g., nitrogen). The data in Figs. 4(a) and 4(b) show the time-domain waveform and spectrum collected using the same instrument; for the teal curves, the enclosure contained ambient air and for the black curves, the enclosure was filled nitrogen gas, thus reducing the relative humidity to ~3%. Although at this humidity there are still some very weak oscillations present in the THz time-domain waveform, their contributions are small and do not significantly impact the dynamic range of the measurements.
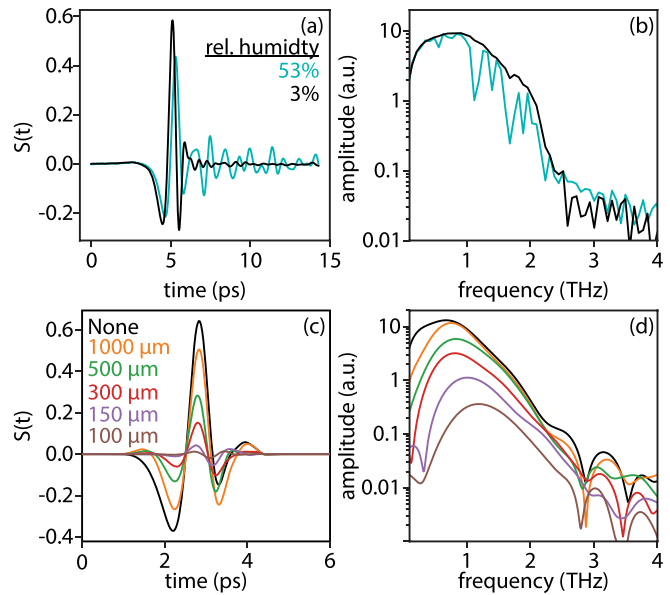
The other key consideration is the effect of the THz spot size. Compared with optical lasers, the long THz wavelength ($300\,\mu m$ at 1 THz) makes tight focusing a challenge because of diffraction effects. This is illustrated in Fig. 4(c), where a series of pinholes with various diameters are placed at the focus of a 3-in. diameter, 3-in. effective-focal-length, $f/1$, 90° off-axis parabolic reflector. Here, even for a $1000\,\mu m$ diameter pinhole, there is a slight reduction in the measured THz field strength as some of the pulse is clipped by the pinhole. This is more apparent for a $500\,\mu m$ diameter pinhole, where the signal has been reduced by almost a factor of two and continues for smaller pinhole diameters. This effect can also be seen in the spectrum, where the lower frequency (longer wavelength) components are more dramatically clipped as they cannot be as tightly focused. This also indicates the importance of ensuring that sample is uniformly driven into the WDM regime and that a large laser spot is used to produce a uniform sample. When using a pump spot that is smaller than the THz probe beam, only the high frequency data will provide reliable information unless the THz pulse can be spatially filtered. This is particularly important when trying to reach extremely high energy density states.

IV. APPLICATIONS FOR WDM STUDIES

Performing single-shot THz measurements on WDM essentially requires combining two different pump-probe setups into one experiment and as such require three different kinds of laser pulses: (1) a drive pulse for exciting the sample, (2) a few mJ femtosecond pulse for making the THz pulse, and (3) a few μJ femtosecond pulse to readout the THz pulse. Different drive pulses can be used to achieve different WDM conditions. For example, pulses with Joule-level energy and tens of nanosecond duration can be used for laser driven compression while pulses with tens to hundreds of millijoule energy and femtosecond

duration can be used for isochoric heating of thin films. For laser based THz generation, optical rectification is often used, and mJ energy pulses are chosen to avoid damaging the optics required. This process yields THz pulses with typically $<1\,\mu J$ pulse energy. In the first pump-probe setup, the sample is driven to the WDM state with an intense or high energy laser pulse, and a time-delayed THz pulse delivered to the sample to probe. The other pump-probe setup is the echelon-based single-shot detection, where the THz pulse is readout as described above. Presently, measurements on WDM can be performed with the THz probing in a transmission geometry[55,57] or in a reflection mode. These two experimental platforms allow for measurements of different parts of WDM phase space—either isochorically heated or under shock compression.

A. Laser-heated thin films

Laser heating films can produce non-equilibrium WDM and study WDM at up-to solid-density conditions.[19,20,70,71] In these experiments, an intense femtosecond laser irradiates a nanometer-thin sample of material, thereby heating the electrons in the material to electronvolt temperatures. The electrons and ions thermalize between 1 and 100 ps, depending on the electron–phonon coupling strength. During this time, a THz pulse can be used to probe the sample. On sufficiently short timescales, the sample will not undergo hydrodynamic expansion, and thus, the THz pulse will probe an isochorically heated material.

1. Experimental setup

A schematic of the experiment is shown in Fig. 5(a). The data presented here were collected using an amplified femtosecond laser system which produced two separate 8 and 5 mJ $\lambda = 800$ nm, 50 fs pulses. The 8 mJ pulse served as the drive, while the 5 mJ pulse was split 90:10 for THz generation, performed by optical rectification in a 2 mm (1 1 0)-cut ZnTe crystal[41–43] and THz detection by single-shot electro-optic sampling described above. The THz pulse was focused to the target plane using the same $f/1$ parabola. The drive pulse was spatially filtered and imaged onto the target plane. Overlap was accomplished by delivering the drive pulse through a 3 mm hole in the parabolic mirror focusing the THz pulse. A mechanical delay stage was used to set the arrival time of the drive pulse relative to the THz pulse. The samples were 40 nm aluminum films.

For data collection, computer-controlled mechanical shutters were used to block and unblock beams to collect echelon images with the THz pulse absent, only the THz pulse present, and both the drive and the THz pulses present. The measured echelon images were used to construct waveforms corresponding to the THz pulse transmitted through an empty hole (the reference), through the cold film, and then the heated material.

Compared with our initial demonstration,[55] the films were deposited onto a thick aluminum plate with 1 mm diameter holes spaced 3 mm apart. This resulted in free-standing films over the 1 mm diameter holes, while the plate acted as a mask and ensured that the THz pulse only probed heated material. The experimental setup was also enclosed in a nitrogen atmosphere. These improvements permit accurate analysis of the THz spectrum, which was not possible previously. The use of $\lambda = 800$ nm pulses enables higher fluences, so targets can be driven to higher energy density WDM states.
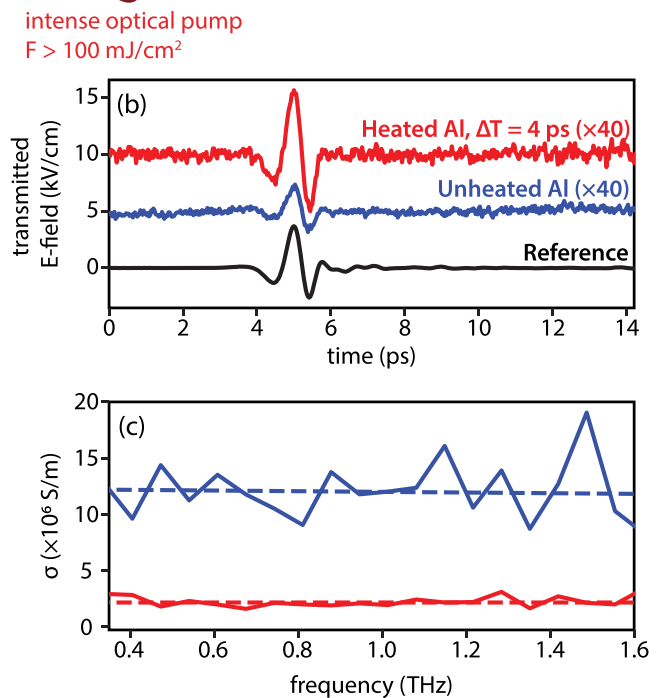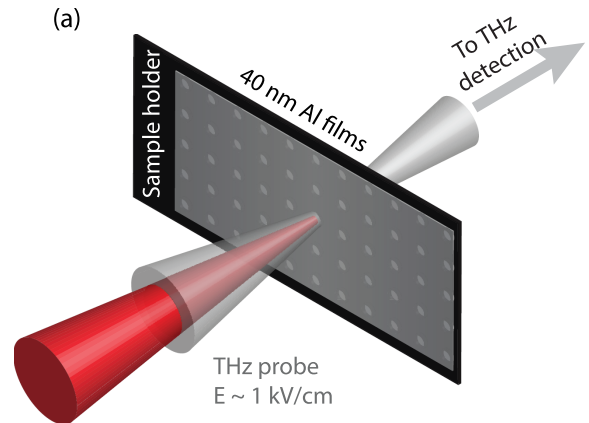
FIG. 5. (a) Schematic of the experimental setup around the sample plane. (b) Time-domain waveforms for the THz pulse, offset for clarity. The data on the cold and heated films are scaled 40×. (c) Frequency-dependent conductivity determined from THz measurements.

Representative waveforms are shown in Fig. 5(b), with the black, blue, and red waveforms corresponding to the THz transmission through an empty hole, the cold film, and the heated film, respectively. The incident drive pulse fluence was ~100 mJ/cm², a factor of two higher than our previous measurements, corresponding to an intensity of 2×10^{12} W/cm², and the THz pulse was delayed by 4 ps. The data clearly show a significant decrease in the THz transmission when the THz pulse passes through the unheated thin film (blue) compared to the 1 mm hole (black). This is expected, as the high conductivity of the film makes it reflective to the THz field. When the film is heated with the drive, the THz transmission increases, indicating a change in the conductivity of the sample.

2. Conductivity determination

To determine the conductivity, the spectrum of the THz pulse transmitted through the film, $\tilde{E}_s(\omega)$ was normalized to the spectrum obtained from the field transmitted through the air hole $\tilde{E}_r(\omega)$. This gives the complex-valued transmission function, $\tilde{t}(\omega) = \tilde{E}_s(\omega)/\tilde{E}_r(\omega)$. For a free-standing thin film, the complex-value conductivity can be calculated using the Tinkham formula,[72] which accounts for multiple reflections of the field within the film,

$$\tilde{\sigma}(\omega) = \frac{2}{Z_0 d}\left(\frac{1}{\tilde{t}(\omega)} - 1\right), \tag{10}$$

where $Z_0 = 377\,\Omega$ is the impedance of free space, and d is the film thickness and was determined independently by frequency-domain interferometry[73–75] to have increased by 20%. The determined $\tilde{\sigma}(\omega)$ are shown in Fig. 5(c) for the unperturbed and heated film. We plot only the real part of the conductivity as the imaginary part is several orders of magnitude smaller. Initially, the film has an average real conductivity of $13 \pm 1 \times 10^6$ S/m, and upon heating into the WDM regime, the conductivity drops to $2.1 \pm 0.3 \times 10^6$ S/m. The details of this change go beyond the scope of this manuscript and a more systematic study will be the subject of future investigations.

B. Dynamically compressed matter

Another common method for producing WDM is by laser-driven shock compression.[21,26] In this technique, a thick (e.g., $<1\,\mu$m) sample is irradiated with high energy nanosecond long laser pulse. The laser sample interaction generates a plasma at the surface of a target which ablates away. Consistent with Newton's third law, this ablation consequently launches a shock wave which drives the material into a high pressure and high temperature state. Typical conditions achieved using laser driven shock compression are in the megabar pressure range. Furthermore, the resultant WDM state can be maintained for the duration of the drive laser pulse (e.g., tens of nanoseconds). During this time, the THz pulse probes the reflectivity opposite to the drive side of the sample.

1. Experimental setup

A schematic highlighting the key elements of a setup for THz probing of the compressed matter is shown in Fig. 6. Data presented here were measured at the Janus Target Area 1 of the Jupiter Laser Facility at Lawrence Livermore National Laboratory. Pulses for generating and measuring the THz pulse were produced by a Coherent Hidra Ti:sapphire amplified laser system that delivered $\lambda = 800$ nm pulses with a duration of 50 fs at 10 Hz repetition rate. The THz pulse was generated using a 2 mm thick ZnTe crystal and directed to the target using a pair of $f/2$ off-axis parabolic reflectors. The focusing THz pulse had an incidence angle of 60° relative to the target normal. The reflected THz pulse was collected and imaged using a matched set of off-axis parabolic reflectors onto a 2 mm ZnTe crystal, where single-shot EO sampling was accomplished using a reflective echelon. The target assembly consisted of a 100 nm layer of Al, a 25 μm CH ablator layer, a second 100 nm layer of Al, and a 500 μm lithium flouride (LiF) window. The 100 nm of Al was coated on the 25 μm CH, and the LiF was glued to the target stack. The THz pulse reflected from the
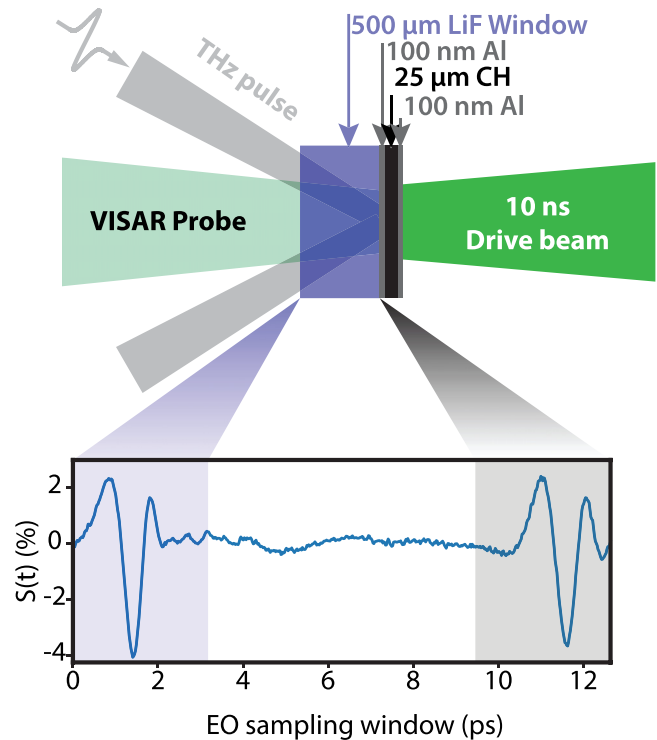

FIG. 6. (a) Schematic of the experimental setup around the sample plane. (b) Time-domain waveform showing two THz pulses. The first is due to the reflection at the vacuum–LiF interface and the second from the LiF–sample interface.

vacuum–LiF and LiF–Al interfaces, while the drive arrived at the exposed 100 nm Al-coated side of the target.

The drive laser was configured to produce 10 ns square pulses with up to 300 J at 2ω ($\lambda = 527$ nm). Continuous phase plates (CPPs) were used to generate a 1 mm diameter spatially averaged uniform-intensity drive spot on the target. The maximum on-target intensity was 3.82×10^{12} W/cm^2. A two channel velocity interferometry system for any reflector (VISAR) was used to determine the shock breakout time and hence shock velocity.[76,77] The arrival time of the THz pulse first calibrated by sending 800 nm pulses that are co-timed with the THz pulse to the target position. The 800 nm pulses were subsequently scattered and collected by the streak cameras in the VISAR system. The drive beam arrival time was calibrated using a reference laser co-timed with the drive laser. This reference laser was similarly directed to target position and the reflected into the VISAR streak cameras. Fiducials were then set on the VISAR streak camera windows to mark the arrival of the THz pulses and the drive laser as shown in Fig. 8. The error in the arrival time, estimated from the width of the fiducial signals, is $\pm$ 30 ps.

2. Data example and data analysis

Unlike the transmission measurements, the time-domain waveforms in Fig. 6(b) show two pulses. These arise from the reflections of the THz pulse at the vacuum–LiF interface and the LiF–aluminum interface. In general, anywhere there is a significant change in the THz refractive index, and this will lead to a pulse appearing in the time

domain. In the undriven measurement, the temporal separation between the pulses is set by the optical path length of the THz pulse through the LiF,

$$\Delta t = \frac{2 n_{LiF} \ell}{c_0 \cos \theta}, \qquad (11)$$

where i_{LiF} is the THz refractive index of LiF at ambient conditions, ℓ is the LiF thickness, c_0 is the speed of light, and θ is the propagation angle of the THz pulse within the LiF relative to the surface normal. Given our measured delay of $\Delta t = 9.8$ ps and $\ell = 500\,\mu$m, we determine a THz frequency refractive index of 2.8 for LiF, in good agreement with previous measurements of ambient LiF.[78]

Though the use of a window material is not mandatory, it has the added benefit that the reflection at the vacuum–LiF interface should not be affected by the shockwave produced at the other side of the sample. As such, the THz pulse reflected at that interface can act as an on-shot reference. This is particularly valuable when there are large shot-to-shot fluctuations in the THz pulse. On-shot referencing may be implemented by correlating the spectrum of the THz pulse reflected at the first interface to that reflected at the second interface. A visual representation of this procedure is shown in Fig. 7. This is based on a similar approach where a THz pulse was split into two, and the separate THz pulses measured at different EO sampling crystals.[79] Here, the time-domain waveform from an undriven measurement was divided so that each THz pulse was isolated, and each pulse was separately Fourier transformed to obtain two THz spectra, $\tilde{E}_{w,0}(\omega)$ and $\tilde{E}_{s,0}(\omega)$, for the vacuum–window and window–sample interfaces, respectively. Next, a correlation function was calculated by using these spectra, $\hat{C}(\omega) = \tilde{E}_{s,0}(\omega)/\tilde{E}_{w,0}(\omega)$. For measurements taken with the

drive, the data were split in the same way, and the reference spectrum was calculated using the correlation function

$$\tilde{E}_{s,r}(\omega) = \tilde{E}_w(\omega)\hat{C}(\omega) = \tilde{E}_w(\omega)\frac{\tilde{E}_{s,0}(\omega)}{\tilde{E}_{w,0}(\omega)}. \qquad (12)$$

Finally, the reflectivity ratio can be calculated as $\tilde{r} = \tilde{E}_s(\omega)/\tilde{E}_{s,r}(\omega)$.

A representative set of data collected during a shot is shown in Fig. 8. The drive energy for this shot was 282 J as measured using calibrated energy meters. Figure 8(a) shows a VISAR trace annotated to
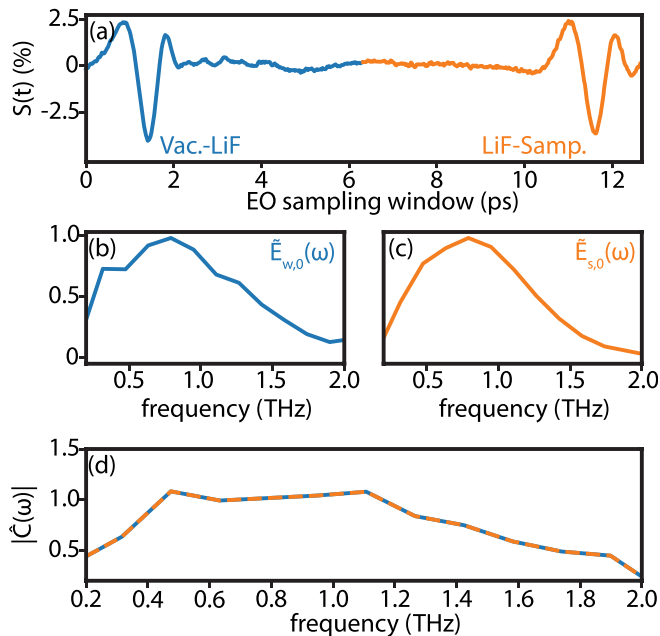

FIG. 7. (a) Time domain waveform of THz pulses measured without drive. Data in blue (left half of the waveform) are used to determine $\tilde{E}_{w,0}$ and data in orange (right half of waveform) provide $\tilde{E}_{s,0}$. Plots of (b) $\tilde{E}_{w,0}$ and (c) $\tilde{E}_{s,0}$. (d) Frequency domain amplitude of $\hat{C}(\omega)$.
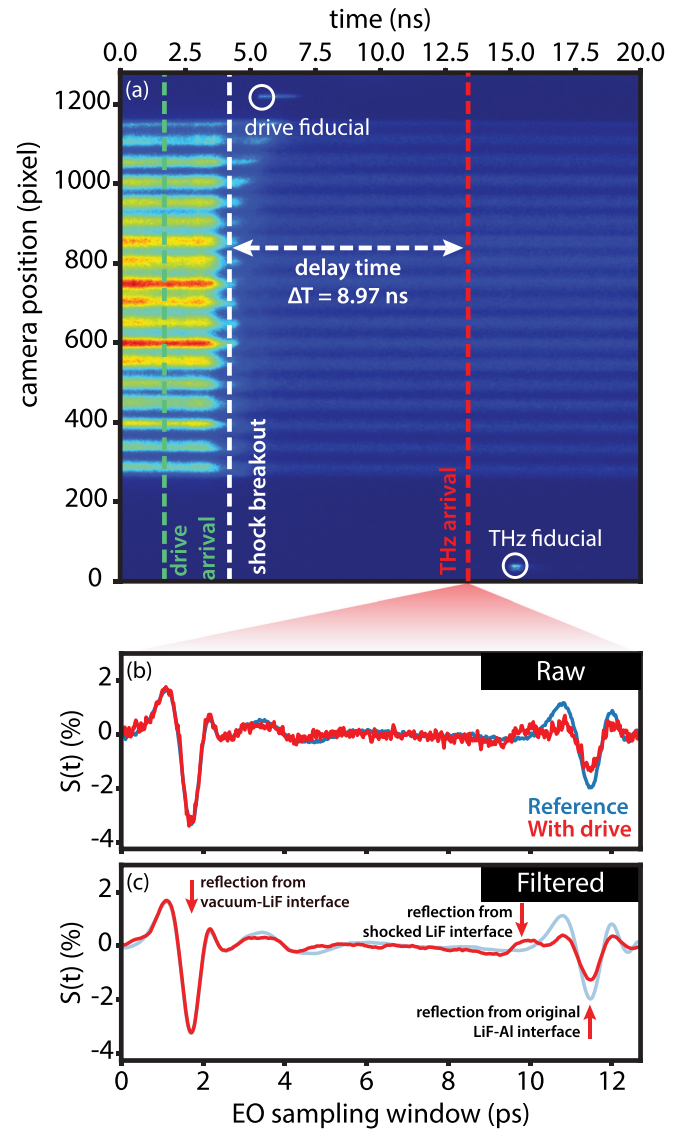
FIG. 8. (a) VISAR image showing fiducials and arrival times of the drive and THz pulses as well as the shock breakout. (b) Raw and (c) filtered time-domain waveforms show THz pulses reflected from vacuum–LiF and LiF–Al interfaces with no drive and with drive present. Data are overlaid to highlight the change in the THz pulse reflected at the original LiF–Al interface. Additionally, a weak THz pulse is seen likely due to changes in optical properties of the LiF.

show the arrival times of the drive laser to the target as well as the THz pulses; these were determined by the positions of the fiducials discussed previously. The VISAR image shows a loss of reflectivity just before 5 ns on the streak camera window, which is attributed to the shock breakout through the 100 nm of Al into the LiF window. For the purpose of this demonstrative work, we only use this change to indicate that the shockwave has passed into the LiF.

Figure 8(b) shows data collected by single-shot EO sampling. The data show measurements taken both with and without the drive present. The reference data are an average of 50 undriven measurements. The "with drive" measurement is a single shot. For the driven measurement, a clear change is visible for the pulse reflected at the original LiF–Al interface, while the pulse at the vacuum–LiF interface overlaps well. This indicates the repeatability of the THz pulse produced for the measurements. Because the Al layer used was only 100 nm, we do not expect a sustained shock in the Al and thicker targets are more appropriate for extracting the conductivity. However, the data still indicate the ability to determine shock induced changes in the THz reflectivity.

Figure 8(c) shows the same data smoothed to remove noise. In the both the reference and driven measurements, THz pulses originating from reflections at the vacuum–LiF and the original LiF–Al interface are present at 1.8 and 11.5 ps, respectively. In the driven measurement, a weaker THz pulse at about 10 ps. This is likely due to a reflection from the shock front in the LiF window, indicating that the optical properties of the LiF have changed. The new pulse arrives earlier than the one reflected at the original LiF–Al interface because the shock has created a new interface within the LiF, effectively reducing ℓ in Eq. (11) and, thus, reducing Δt.

For a sufficiently thick sample, the conductivity of the compressed material can be determined starting from the Fresnel relation for reflectivity:[80]

$$\tilde{r}_p = \frac{\tilde{n}_w \sqrt{1 - \left(\frac{\tilde{n}_w}{\tilde{n}_s}\right)^2 \sin^2(\theta)} - \tilde{n}_s \cos(\theta)}{\tilde{n}_w \sqrt{1 - \left(\frac{\tilde{n}_w}{\tilde{n}_s}\right)^2 \sin^2(\theta)} + \tilde{n}_s \cos(\theta)}, \quad (13)$$

where $\tilde{r}_p$ is the measured reflectivity assuming a p-polarized THz field, $\tilde{n}_w$ is the refractive index of the window, $\tilde{n}_s$ is the refractive index of the sample, and θ is the angle of incidence of the pulse at the window-sample interface. In the case that $\tilde{n}_w \ll \tilde{n}_s$, this expression can be approximated by

$$\tilde{r}_p \approx \frac{\tilde{n}_w - \tilde{n}_s \cos(\theta)}{\tilde{n}_w + \tilde{n}_s \cos(\theta)}. \quad (14)$$

In this form, the expression can be inverted to solve for the refractive index of the sample,

$$\tilde{n}_s = \frac{1 - \tilde{r}_p}{1 + \tilde{r}_p} \frac{\tilde{n}_w}{\cos\theta}. \quad (15)$$

For WDM where there are a large number of free electrons, we can relate the refractive index to the conductivity by

$$\tilde{\sigma}(\omega) = -i\omega\varepsilon_0 \left(\tilde{n}_s^2(\omega) - 1\right). \quad (16)$$

From this, we see that knowledge of $\tilde{n}_w$ is required to determine the conductivity accurately, which is not yet determined in the THz regime at shocked conditions. Changes in the refractive index of LiF have been observed using visible and infrared frequency light.[81] However, there is no evidence of a correlation between those changes and what would be expected at THz frequencies. Separate measurements are required to determine the relevant refractive indices at THz frequencies and those along with experiments with thicker targets will be the focus of future studies.

V. CONCLUSIONS AND OUTLOOK

In conclusion, we have presented the details of single-shot THz measurements on WDM and provided details of demonstrative experiments illustrating the technique. A reflective echelon enables THz time-domain waveforms to be recorded in a single shot with a high signal-to-noise, thus enabling spectroscopic characterization of materials driven in to the WDM regime. We describe details of the design of our experiments to optimize the signal-to-noise ratio and show the results of experiments where single cycle THz pulses are used to characterize WDM produced by isochoric heating and shock compression. In both cases, the electrical conductivity decreases when driven to the WDM regime and can be calculated from the measurements.

Many areas for improvement exist for making THz studies on WDM. Laser based sources offer a variety of different methods for producing THz radiation.[82] While not discussed, the work here exclusively used ZnTe as a THz source through optical rectification, a process that uses the interaction of an ultrafast pulse a non-linear crystal to produce THz radiation. Lithium niobate has been used as a non-linear crystal to produce intense THz pulses;[83–86] however, the resulting THz pulses have a longer duration than those produced by ZnTe, reducing the temporal resolution of the measurement. An active area of research is the synthesis of new materials for use,[87,88] which could improve the THz field strength or the bandwidth. In particular, N-benzyl-2-methyl-4-nitroaniline (BNA) has been shown to produce intense THz pulses with comparable duration to that of ZnTe. Furthermore, intense laser–matter interactions can produce intense THz radiation,[89–91] facilitating WDM experiments with currently available facilities. While the measurements discussed focus on solid samples, the use of liquid jets[92] offers possibilities for introducing different kinds of samples and also for high repetition rate experiments. Finally, this diagnostic can be combined with x-ray free electron lasers, enabling simultaneous determination of multiple parameters (e.g., conductivity via THz measurements, density via x-ray diffraction, electron temperature via XRTS) and, thus, providing an exciting avenue for characterizing WDM.

ACKNOWLEDGMENTS

AUTHOR DECLARATIONS
Conflict of Interest

The authors have no conflicts to disclose.

09 May 2024 11:47:17

Author Contributions

Benjamin Ofori-Okai: Conceptualization (lead); Data curation (lead); Formal analysis (lead); Investigation (lead); Methodology (lead); Software (lead); Visualization (lead); Writing—original draft (lead); Writing—review & editing (lead). **Siegfried Glenzer:** Conceptualization (equal); Funding acquisition (lead); Supervision (lead); Writing—review & editing (equal). **Adrien Descamps:** Investigation (equal); Writing—review & editing (equal). **Emma Elizabeth McBride:** Conceptualization (equal); Investigation (equal); Writing—review & editing (equal). **Mianzhen Mo:** Investigation (equal); Writing—review & editing (equal). **Anthea Weinmann:** Investigation (equal); Writing—review & editing (equal). **Lars Seipp:** Investigation (equal); Writing—review & editing (equal). **Suzanne Jihad Ali:** Investigation (equal); Writing—review & editing (equal). **Zhijiang Chen:** Conceptualization (equal); Investigation (equal); Methodology (equal); Writing—review & editing (equal). **Luke Bennett Fletcher:** Conceptualization (equal); Investigation (equal); Writing—review & editing (equal).

DATA AVAILABILITY

The data that support the findings of this study are available from the corresponding author upon reasonable request.

APPENDIX: THE POCKELS EFFECT FOR EO SAMPLING

Here, we derive the expressions for Eqs. (2a)–(2c). The change in the refractive index via the Pockels effect is described by considering the optical impermeability tensor, $\bar{\bar{\eta}}$, a 3×3 rank 2 tensor whose elements are the inverse of the elements of the dielectric tensor $\bar{\bar{\varepsilon}}$ (i.e., $\eta_{ij} = 1/\varepsilon_{ij}$). Combined with the relationship between the dielectric constant and the refractive index, $\varepsilon_{ij} = n_{ij}^2$,

$$\bar{\bar{\eta}} = \begin{bmatrix} \eta_{xx} & \eta_{xy} & \eta_{xz} \\ \eta_{yx} & \eta_{yy} & \eta_{yz} \\ \eta_{zx} & \eta_{zy} & \eta_{zz} \end{bmatrix} = \begin{bmatrix} 1/n_{xx}^2 & 1/n_{xy}^2 & 1/n_{xz}^2 \\ 1/n_{yx}^2 & 1/n_{yy}^2 & 1/n_{yz}^2 \\ 1/n_{zx}^2 & 1/n_{zy}^2 & 1/n_{zz}^2 \end{bmatrix}. \quad (A1)$$

For a lossless medium, $\bar{\bar{\eta}}$ is a symmetric matrix (i.e., $\eta_{ji} = \eta_{ij}$). When any of the elements is modified, one can then write the modified elements of the impermeability tensor as

$$\eta_{ij} = \eta_{ij,0} + \Delta\eta_{ij} = \frac{1}{n_{ij,0}^2} + \Delta\left(\frac{1}{n_{ij}^2}\right), \quad (A2)$$

where $\eta_{ij,0}$ is the original impermeability tensor element, $\Delta\eta_{ij}$ is the change in that element, and $n_{ij,0}$ and $\Delta(1/n_{ij})^2$ are the associated refractive index and its change. If the impermeability tensor is diagonal, the elements can be used to derive the following expressions for the change in the refractive index:

$$\Delta n_{ii} = -\frac{1}{2}n_{ii}^3 \Delta\eta_{ii}. \quad (A3)$$

The applied electric field from the THz pulse, $\vec{E}_{THz} = E_x\hat{x} + E_y\hat{y} + E_z\hat{z}$, changes the impermeability according to

$$\begin{bmatrix} \Delta\bar{\bar{\eta}}_{xx} \\ \Delta\bar{\bar{\eta}}_{yy} \\ \Delta\bar{\bar{\eta}}_{zz} \\ \Delta\bar{\bar{\eta}}_{yz} \\ \Delta\bar{\bar{\eta}}_{xz} \\ \Delta\bar{\bar{\eta}}_{xy} \end{bmatrix} = \begin{bmatrix} r_{11} & r_{12} & r_{13} \\ r_{21} & r_{22} & r_{23} \\ r_{31} & r_{32} & r_{33} \\ r_{41} & r_{42} & r_{43} \\ r_{51} & r_{52} & r_{53} \\ r_{61} & r_{62} & r_{63} \end{bmatrix} \begin{bmatrix} E_x \\ E_y \\ E_z \end{bmatrix}, \quad (A4)$$

where the 3×6 matrix is the electro-optic tensor with r_{ij} as its elements.

The details of the EO tensor and the impermeability are determined from the symmetry and cut of the EO crystal. For ZnTe or GaP crystals, the dielectric and impermeability tensors are diagonal, with $\varepsilon_{ii} = \varepsilon_0$. The only nonzero elements of the EO tensor are $r_{41} = r_{52} = r_{63}$. In the case presented, the crystal is cut along the (1 1 0) planes, with the z-axis set parallel to the [0 0 1] crystallographic axis. In this geometry, the THz field can be written as $\vec{E}_{THz} = E_{THz}(\sin(\alpha)/\sqrt{2}\hat{x} - \sin(\alpha)/\sqrt{2}\hat{y} + \cos(\alpha)\hat{z})$. When such a field is applied, the impermeability tensors becomes

$$\bar{\bar{\eta}} = \begin{bmatrix} \eta_0 & \Delta\eta_{xy} & \Delta\eta_{xz} \\ \Delta\eta_{xy} & \eta_0 & \Delta\eta_{yz} \\ \Delta\eta_{xz} & \Delta\eta_{yz} & \eta_0 \end{bmatrix}, \quad (A5)$$

where the modifying terms are defined as

$$\Delta\eta_{xx} = \Delta\eta_{yy} = \Delta\eta_{zz} = 0, \quad (A6a)$$

$$\Delta\eta_{yz} = -\Delta\eta_{xz} = \frac{1}{\sqrt{2}}r_{41}E_{THz}\sin(\alpha), \quad (A6b)$$

$$\Delta\eta_{xy} = r_{41}E_{THz}\cos(\alpha). \quad (A6c)$$

In order to determine how the refractive indices of the crystal are modified, this matrix needs to be diagonalized. For this configuration, this is accomplished by first applying a 45° clockwise rotation matrix around the z-axis, yielding the following impermeability matrix:

$$\begin{bmatrix} \eta_0 + \Delta\eta_{xy} & 0 & 0 \\ 0 & \eta_0 - \Delta\eta_{xy} & \Delta\eta_{yz}\sqrt{2} \\ 0 & \Delta\eta_{yz}\sqrt{2} & \eta_0 \end{bmatrix}. \quad (A7)$$

This places the [1 1 0] axis along the x-axis and reflects the use of a (1 1 0)-cut for the EO crystal. The form of this matrix indicates that the fast and slow axes are rotated around the current x-axis by an angle ψ, which can be determined diagonalizing this matrix. To do this, a second rotation about the x-axis is applied, yielding an impermeability matrix

$$\begin{bmatrix} \eta_0 + \Delta\eta_{xy} & 0 & 0 \\ 0 & \eta_0 + \Delta\eta_{yz}\sqrt{2}\sin(2\psi) - \Delta\eta_{xy}\cos^2(\psi) & \sqrt{2}\Delta\eta_{yz}\cos(2\psi) + \frac{1}{2}\Delta\eta_{xy}\sin(2\psi) \\ 0 & \sqrt{2}\Delta\eta_{yz}\cos(2\psi) + \frac{1}{2}\Delta\eta_{xy}\sin(2\psi) & \eta_0 - \sqrt{2}\Delta\eta_{yz}\sin(2\psi) - \Delta\eta_{xy}\sin^2(\psi) \end{bmatrix}. \quad (A8)$$

09 May 2024 11:47:17

In order for this matrix to be diagonalized, ψ should be chosen such that the off-diagonal elements are zero. Substituting for $\Delta\eta_{xy}$ and $\Delta\eta_{xz}$, the off-diagonal terms become

$$r_{41}E_{\mathrm{THz}}\left[\sin\left(\alpha\right)\cos\left(2\psi\right)+\frac{1}{2}\cos\left(\alpha\right)\sin\left(2\psi\right)\right]. \qquad (A9)$$

Setting this term to zero yields Eq. (3), thereby defining the relationship between α and ψ.

REFERENCES

[1]J. D. Lindl, "Development of the indirect-drive approach to inertial confinement fusion and the target physics basis for ignition and gain," Phys. Plasmas **2**, 3933–4024 (1995).

[2]J. D. Lindl, P. Amendt, R. L. Berger, S. G. Glendinning, S. H. Glenzer, S. W. Haan, R. L. Kauffman, O. L. Landen, and L. J. Suter, "The physics basis for ignition using indirect-drive targets on the National Ignition Facility," Phys. Plasmas **11**, 339–491 (2004).

[3]N. Nettelmann, A. Becker, B. Holst, and R. Redmer, "Jupiter models with improved ab initio hydrogen equation of state (H-REOS.2)," Astrophys. J. **750**, 52 (2012).

[4]M. French, A. Becker, W. Lorenzen, N. Nettelmann, M. Bethkenhagen, J. Wicht, and R. Redmer, "Ab initio simulations for material properties along the Jupiter adiabat," Astrophys. J., Suppl. Ser. **202**, 5 (2012).

[5]R. P. Drake, *High-Energy-Density Physics*, Shock Wave and High Pressure Phenomena, edited by L. Davison and Y. Horie (Springer Berlin Heidelberg, 2006).

[6]R. P. Drake, "Perspectives on high-energy-density physics," Phys. Plasmas **16**, 055501 (2009).

[7]T. Ma, L. B. Fletcher, A. Pak, D. A. Chapman, R. W. Falcone, C. Fortmann, E. Galtier, D. O. Gericke, G. Gregori, J. Hastings, O. L. Landen, S. Le Pape, H. J. Lee, B. Nagler, P. Neumayer, D. Turnbull, J. Vorberger, T. G. White, K. Wünsch, U. Zastrau, S. H. Glenzer, and T. Döppner, "Observations of strong ion–ion correlations in dense plasmas," Phys. Plasmas **21**, 056302 (2014).

[8]L. Spitzer and R. Härm, "Transport phenomena in a completely ionized gas," Phys. Rev. **89**, 977–981 (1953).

[9]R. Kubo, "Statistical-mechanical theory of irreversible processes. I. General theory and simple applications to magnetic and conduction problems," J. Phys. Soc. Jpn. **12**, 570–586 (1957).

[10]J. M. Ziman, "A theory of the electrical properties of liquid metals. I: The monovalent metals," Philos. Mag. **6**, 1013–1034 (1961).

[11]Y. T. Lee and R. M. More, "An electron conductivity model for dense plasmas," Phys. Fluids **27**, 1273 (1984).

[12]R. Redmer, "Electrical conductivity of dense metal plasmas," Phys. Rev. E **59**, 1073–1081 (1999).

[13]B. B. L. Witte, L. B. Fletcher, E. Galtier, E. J. Gamboa, H. J. Lee, U. Zastrau, R. Redmer, S. H. Glenzer, and P. Sperling, "Warm dense matter demonstrating non-drude conductivity from observations of nonlinear plasmon damping," Phys. Rev. Lett. **118**, 225001 (2017).

[14]M. W. C. Dharma-wardana, D. D. Klug, L. Harbour, and L. J. Lewis, "Isochoric, isobaric, and ultrafast conductivities of aluminum, lithium, and carbon in the warm dense matter regime," Phys. Rev. E **96**, 053206 (2017).

[15]B. B. L. Witte, P. Sperling, M. French, V. Recoules, S. H. Glenzer, and R. Redmer, "Observations of non-linear plasmon damping in dense plasmas," Phys. Plasmas **25**, 056901 (2018).

[16]M. Schörner, B. B. Witte, A. D. Baczewski, A. Cangi, and R. Redmer, "Ab initio study of shock-compressed copper," Phys. Rev. B **106**, 054304 (2022).

[17]T. Dornheim, Z. A. Moldabekov, K. Ramakrishna, P. Tolias, A. D. Baczewski, D. Kraus, T. R. Preston, D. A. Chapman, M. P. Böhme, T. Döppner, F. Graziani, M. Bonitz, A. Cangi, and J. Vorberger, "Electronic density response of warm dense matter," Phys. Plasmas **30**, 032705 (2023).

[18]U. Kleinschmidt, M. French, G. Steinle-Neumann, and R. Redmer, "Electrical and thermal conductivity of fcc and hcp iron under conditions of the Earth's core from ab initio simulations," Phys. Rev. B **107**, 085145 (2023).

[19]A. Ng, T. Ao, F. Perrot, M. W. Dharma-Wardana, and M. E. Foord, "Idealized slab plasma approach for the study of warm dense matter," Laser Part. Beams **23**, 527–537 (2005).

[20]Z. Chen, B. Holst, S. E. Kirkwood, V. Sametoglu, M. Reid, Y. Y. Tsui, V. Recoules, and A. Ng, "Evolution of ac conductivity in nonequilibrium warm dense gold," Phys. Rev. Lett. **110**, 135001 (2013).

[21]L. B. Fletcher, H. J. Lee, T. Döppner, E. Galtier, B. Nagler, P. Heimann, C. Fortmann, S. LePape, T. Ma, M. Millot, A. Pak, D. Turnbull, D. A. Chapman, D. O. Gericke, J. Vorberger, T. White, G. Gregori, M. Wei, B. Barbrel, R. W. Falcone, C.-C. Kao, H. Nuhn, J. Welch, U. Zastrau, P. Neumayer, J. B. Hastings, and S. H. Glenzer, "Ultrabright X-ray laser scattering for dynamic warm dense matter physics," Nat. Photonics **9**, 274–279 (2015).

[22]M. Millot, N. A. Dubrovinskaia, S. Blaha, L. S. Dubrovinsky, D. G. Braun, P. M. Celliers, G. W. Collins, J. H. Eggert, and R. Jeanloz, "Shock compression of stishovite and melting of silica at planetary interior conditions," Science **347**, 418 (2015).

[23]D. Kraus, J. Vorberger, A. Pak, N. J. Hartley, L. B. Fletcher, S. Frydrych, E. Galtier, E. J. Gamboa, D. O. Gericke, S. H. Glenzer, E. Granados, M. J. MacDonald, A. J. MacKinnon, E. E. McBride, I. Nam, P. Neumayer, M. Roth, A. M. Saunders, A. K. Schuster, P. Sun, T. Van Driel, T. Döppner, and R. W. Falcone, "Formation of diamonds in laser-compressed hydrocarbons at planetary interior conditions," Nat. Astron. **1**, 606–611 (2017).

[24]M. Millot, S. Hamel, J. R. Rygg, P. M. Celliers, G. W. Collins, F. Coppari, D. E. Fratanduono, R. Jeanloz, D. C. Swift, and J. H. Eggert, "Experimental evidence for superionic water ice using shock compression," Nat. Phys. **14**, 297–302 (2018).

[25]M. Z. Mo, V. Becker, B. K. Ofori-Okai, X. Shen, Z. Chen, B. B. L. Witte, R. Redmer, R. K. Li, M. Dunning, S. P. Weathersby, X. J. Wang, and S. H. Glenzer, "Determination of the electron-lattice coupling strength of copper with ultrafast MeV electron diffraction," Rev. Sci. Instrum. **89**, 10C108 (2018).

[26]E. E. McBride, A. Krygier, A. Ehnes, E. Galtier, M. Harmand, Z. Konôpková, H. J. Lee, H.-P. Liermann, B. Nagler, A. Pelka, M. Rödel, A. Schropp, R. F. Smith, C. Spindloe, D. Swift, F. Tavella, S. Toleikis, T. Tschentscher, J. S. Wark, and A. Higginbotham, "Phase transition lowering in dynamically compressed silicon," Nat. Phys. **15**, 89–94 (2019).

[27]H. M. Milchberg, R. R. Freeman, S. C. Davey, and R. M. More, "Resistivity of a simple metal from room temperature to 10^6 K," Phys. Rev. Lett. **61**, 2364–2367 (1988).

[28]D. G. Hicks, T. R. Boehly, J. H. Eggert, J. E. Miller, P. M. Celliers, and G. W. Collins, "Dissociation of liquid silica at high pressures and temperatures," Phys. Rev. Lett. **97**, 025502 (2006).

[29]S. J. Ali, C. A. Bolme, G. W. Collins, and R. Jeanloz, "Development of a broad-band reflectivity diagnostic for laser driven shock compression experiments," Rev. Sci. Instrum. **86**, 043112 (2015).

[30]A. Ng, P. Sterne, S. Hansen, V. Recoules, Z. Chen, Y. Y. Tsui, and B. Wilson, "dc conductivity of two-temperature warm dense gold," Phys. Rev. E **94**, 033213 (2016).

[31]Z. Chen, X. Na, C. B. Curry, S. Liang, M. French, A. Descamps, D. P. Deponte, J. D. Koralek, J. B. Kim, S. Lebovitz, M. Nakatsutsumi, B. K. Ofori-Okai, R. Redmer, C. Roedel, M. Schörner, S. Skruszewicz, P. Sperling, S. Toleikis, M. Z. Mo, and S. H. Glenzer, "Observation of a highly conductive warm dense state of water with ultrafast pump-probe free-electron-laser measurements," Matter Radiat. Extremes **6**, 054401 (2021).

[32]S. H. Glenzer and R. Redmer, "X-ray Thomson scattering in high energy density plasmas," Rev. Mod. Phys. **81**, 1625–1663 (2009).

[33]P. Sperling, E. J. Gamboa, H. J. Lee, H. K. Chung, E. Galtier, Y. Omarbakiyeva, H. Reinholz, G. Röpke, U. Zastrau, J. Hastings, L. B. Fletcher, and S. H. Glenzer, "Free-electron X-ray laser measurements of collisional-damped plasmons in isochorically heated warm dense matter," Phys. Rev. Lett. **115**, 115001 (2015).

[34]P. Sperling, S. Rosmej, R. Bredow, L. B. Fletcher, E. Galtier, E. J. Gamboa, H. J. Lee, H. Reinholz, G. Röpke, U. Zastrau, and S. H. Glenzer, "Electrical conductivity calculations in isochorically heated warm dense aluminum," J. Phys. B **50**, 134002 (2017).

[35]C. A. Schmuttenmaer, "Exploring dynamics in the far-infrared with terahertz spectroscopy," Chem. Rev. **104**, 1759–1779 (2004).

[36]J. Neu and C. A. Schmuttenmaer, "Tutorial: An introduction to terahertz time domain spectroscopy (THz-TDS)," J. Appl. Phys. **124**, 231101 (2018).

[37]M. Koch, D. M. Mittleman, J. Ornik, and E. Castro-Camus, "Terahertz time-domain spectroscopy," Nat. Rev. Methods Primers **3**, 48 (2023).

[38]N. W. Ashcroft and N. D. Mermin, *Solid State Physics*, 1st ed. (Brooks/Cole, Belmont, CA, 1976).

[39]Q. Wu and X.-C. Zhang, "Free-space electro-optic sampling of terahertz beams," Appl. Phys. Lett. **67**, 3523–3525 (1995).

[40]A. Nahata, D. H. Auston, T. F. Heinz, and C. Wu, "Coherent detection of freely propagating terahertz radiation by electro-optic sampling," Appl. Phys. Lett. **68**, 150–152 (1996).

[41]A. Nahata, A. S. Weling, and T. F. Heinz, "A wideband coherent terahertz spectroscopy system using optical rectification and electro-optic sampling," Appl. Phys. Lett. **69**, 2321–2323 (1996).

[42]L. Xu, X. C. Zhang, and D. H. Auston, "Terahertz beam generation by femtosecond optical pulses in electro-optic materials," Appl. Phys. Lett. **61**, 1784–1786 (1992).

[43]A. Rice, Y. Jin, X. F. Ma, X. C. Zhang, D. Bliss, J. Larkin, and M. Alexander, "Terahertz optical rectification from ⟨110⟩ zinc-blende crystals," Appl. Phys. Lett. **64**, 1324–1326 (1994).

[44]M. Gensch, L. Bittner, A. Chesnov, H. Delsim-Hashemi, M. Drescher, B. Faatz, J. Feldhaus, U. Fruehling, G. A. Geloni, C. Gerth, O. Grimm, U. Hahn, M. Hesse, S. Kapitzki, V. Kocharyan, O. Kozlov, E. Matyushevsky, N. Morozov, D. Petrov, E. Ploenjes, M. Roehling, J. Rossbach, E. L. Saldin, B. Schmidt, P. Schmueser, E. A. Schneidmiller, E. Syresin, A. Willner, and M. V. Yurkov, "New infrared undulator beamline at FLASH," Infrared Phys. Technol. **51**, 423–425 (2008).

[45]B. A. Knyazev, G. N. Kulipanov, and N. A. Vinokurov, "Novosibirsk terahertz free electron laser: Instrumentation development and experimental achievements," Meas. Sci. Technol. **21**, 054017 (2010).

[46]M. Gensch, B. Green, S. Kovalev, M. Kuntzsch, J. Hauser, R. Schurig, U. Lehnert, P. Michel, A. Al-Shemmary, V. Asgekar, T. Golz, S. Vilcins, H. Schlarb, N. Stojanovic, A. S. Fisher, M. Schwarz, A. S. Mueller, N. Neumann, D. Plettemeier, and G. A. Geloni, "THz facility at ELBE: A versatile test facility for electron bunch diagnostics on QUASI-CW electron beams," in *IPAC 2014: Proceedings of the Fifth International Particle Accelerator Conference* (JACoW Publishing, 2014), pp. 933–934.

[47]R. Pan, E. Zapolnova, T. Golz, A. J. Krmpot, M. D. Rabasovic, J. Petrovic, V. Asgekar, B. Faatz, F. Tavella, A. Perucchi, S. Kovalev, B. Green, G. Geloni, T. Tanikawa, M. Yurkov, E. Schneidmiller, M. Gensch, and N. Stojanovic, "Photon diagnostics at the FLASH THz beamline," J. Synchrotron Radiat. **26**, 700–707 (2019).

[48]A. Fisher, Y. Park, M. Lenz, A. Ody, R. Agustsson, T. Hodgetts, A. Murokh, and P. Musumeci, "Single-pass high-efficiency terahertz free-electron laser," Nat. Photonics **16**, 441–447 (2022).

[49]R. Ulbricht, E. Hendry, J. Shan, T. F. Heinz, and M. Bonn, "Carrier dynamics in semiconductors studied with time-resolved terahertz spectroscopy," Rev. Mod. Phys. **83**, 543–586 (2011).

[50]P. Han, X. Wang, and Y. Zhang, "Time–resolved terahertz spectroscopy studies on 2D Van der Waals materials," Adv. Opt. Mater. **8**, 1900533 (2020).

[51]J. A. Spies, J. Neu, U. T. Tayvah, M. D. Capobianco, B. Pattengale, S. Ostresh, and C. A. Schmuttenmaer, "Terahertz spectroscopy of emerging materials," J. Phys. Chem. C **124**, 22335–22346 (2020).

[52]E. Cinquanta, E. A. A. Pogna, L. Gatto, S. Stagira, and C. Vozzi, "Charge carrier dynamics in 2D materials probed by ultrafast THz spectroscopy," Adv. Phys. **8**, 2120416 (2023).

[53]S. M. S. Teo, B. K. Ofori-Okai, C. C. A. Werley, and K. A. K. Nelson, "Invited article: Single-shot THz detection techniques optimized for multidimensional THz spectroscopy," Rev. Sci. Instrum. **86**, 051301 (2015).

[54]Y. Minami, Y. Hayashi, J. Takeda, and I. Katayama, "Single-shot measurement of a terahertz electric-field waveform using a reflective echelon mirror," Appl. Phys. Lett. **103**, 051103 (2013).

[55]B. K. Ofori-Okai, A. Descamps, J. Lu, L. E. Seipp, A. Weinmann, S. H. Glenzer, and Z. Chen, "Toward quasi-DC conductivity of warm dense matter measured by single-shot terahertz spectroscopy," Rev. Sci. Instrum. **89**, 10D109 (2018).

[56]S. W. Teitelbaum, B. K. Ofori-Okai, Y. H. Y.-H. Cheng, J. Zhang, F. Jin, W. Wu, R. D. Averitt, and K. A. K. Nelson, "Dynamics of a persistent insulator-to-metal transition in strained manganite films," Phys. Rev. Lett. **123**, 267201 (2019).

[57]Z. Chen, C. B. Curry, R. Zhang, F. Treffert, N. Stojanovic, S. Toleikis, R. Pan, M. Gauthier, E. Zapolnova, L. E. Seipp, A. Weinmann, M. Z. Mo, J. B. Kim, B. L. Witte, S. Bajt, S. Usenko, R. Soufli, T. Pardini, S. Hau-Riege, C. Burcklen, J. Schein, R. Redmer, Y. Y. Tsui, B. K. Ofori-Okai, and S. H. Glenzer, "Ultrafast multi-cycle terahertz measurements of the electrical conductivity in strongly excited solids," Nat. Commun. **12**, 1638 (2021).

[58]Q. Wu and X.-C. Zhang, "Broadband detection capability of ZnTe electro-optic field detectors," Appl. Phys. Lett. **68**, 2924–2926 (1996).

[59]G. Gallot and D. Grischkowsky, "Electro-optic detection of terahertz radiation," J. Opt. Soc. Am. B **16**, 1204–1212 (1999).

[60]P. C. M. Planken, H.-K. Nienhuys, H. J. Bakker, and T. Wenckebach, "Measurement and calculation of the orientation dependence of terahertz pulse detection in ZnTe," J. Opt. Soc. Am. B **18**, 313–317 (2001).

[61]N. C. J. van der Valk, T. Wenckebach, and P. C. M. Planken, "Full mathematical description of electro-optic detection in optically isotropic crystals," J. Opt. Soc. Am. B **21**, 622–631 (2004).

[62]A. Yariv, *Quantum Electronics* (Wiley, 1975).

[63]A. Yariv and P. Yeh, *Photonics: Optical Electronics in Modern Communications*, The Oxford Series in Electrical and Computer Engineering (Oxford University Press, New York, NY, 2007).

[64]R. W. Boyd, "Chapter 11—The electrooptic and photorefractive effects," in *Nonlinear Optics*, 3rd ed. (Academic Press, 2008), Chap. 11, pp. 511–541.

[65]Q. Wu and X. C. Zhang, "Ultrafast electro-optic field sensors," Appl. Phys. Lett. **68**, 1604–1606 (1996).

[66]C. A. Werley, S. M. Teo, and K. A. Nelson, "Pulsed laser noise analysis and pump-probe signal detection with a data acquisition card," Rev. Sci. Instrum. **82**, 123108 (2011).

[67]K. Katayama, H. Inoue, H. Sugiya, Q. Shen, T. Toyoda, and K. a Nelson, "Generation and detection of tunable phonon polaritons using a single transmission grating," Appl. Phys. Lett. **92**, 031906 (2008).

[68]M. Van Exter and D. Grischkowsky, "Carrier dynamics of electrons and holes in moderately doped silicon," Phys. Rev. B **41**, 12140–12149 (1990).

[69]D. M. Slocum, E. J. Slingerland, R. H. Giles, and T. M. Goyette, "Atmospheric absorption of terahertz radiation and water vapor continuum effects," J. Quant. Spectrosc. Radiat. Transfer **127**, 49–63 (2013).

[70]M. Z. Mo, Z. Chen, R. K. Li, M. Dunning, B. B. L. Witte, J. K. Baldwin, L. B. Fletcher, J. B. Kim, A. Ng, R. Redmer, A. H. Reid, P. Shekhar, X. Z. Shen, M. Shen, K. Sokolowski-Tinten, Y. Y. Tsui, Y. Q. Wang, Q. Zheng, X. J. Wang, and S. H. Glenzer, "Heterogeneous to homogeneous melting transition visualized with ultrafast electron diffraction," Science **360**, 1451–1455 (2018).

[71]A. Descamps, B. K. Ofori-Okai, O. Bistoni, Z. Chen, E. Cunningham, L. B. Fletcher, N. J. Hartley, J. B. Hastings, D. Khaghani, M. Mo, B. Nagler, V. Recoules, R. Redmer, M. Schörner, D. G. Senesky, P. Sun, H.-E. Tsai, T. G. White, S. H. Glenzer, and E. E. McBride, "Evidence for phonon hardening in laser-excited gold using x-ray diffraction at a hard x-ray free electron laser," Sci. Adv. **10**, eadh5272 (2024).

[72]M. Tinkham, "Energy gap interpretation of experiments on infrared transmission through superconducting films," Phys. Rev. **104**, 845–846 (1956).

[73]E. Tokunaga, T. Kobayashi, and A. Terasaki, "Frequency-domain interferometer for femtosecond time-resolved phase spectroscopy," Opt. Lett. **17**, 1131 (1992).

[74]J. P. Geindre, A. Mysyrowicz, A. D. Santos, P. Audebert, A. Rousse, G. Hamoniaux, A. Antonetti, F. Falliès, and J. C. Gauthier, "Frequency-domain interferometer for measuring the phase and amplitude of a femtosecond pulse probing a laser-produced plasma," Opt. Lett. **19**, 1997 (1994).

[75]T. Ao, Y. Ping, K. Widmann, D. F. Price, E. Lee, H. Tam, P. T. Springer, and A. Ng, "Optical properties in nonequilibrium phase transitions," Phys. Rev. Lett. **96**, 055001 (2014).

[76]L. M. Barker and R. E. Hollenbach, "Laser interferometer for measuring high velocities of any reflecting surface," J. Appl. Phys. **43**, 4669–4675 (1972).

[77]P. M. Celliers, D. K. Bradley, G. W. Collins, D. G. Hicks, T. R. Boehly, and W. J. Armstrong, "Line-imaging velocimeter for shock diagnostics at the OMEGA laser facility," Rev. Sci. Instrum. **75**, 4916–4929 (2004).

[78]M. Gottlieb, "Optical properties of lithium fluoride in the infrared," J. Opt. Soc. Am. **50**, 343–349 (1960).

[79]B. K. Russell, B. K. Ofori-Okai, Z. Chen, M. C. Hoffmann, Y. Y. Tsui, and S. H. Glenzer, "Self-referenced single-shot THz detection," Opt. Express **25**, 16140–16150 (2017).

09 May 2024 11:47:17

[80]B. E. A. Saleh and M. C. Teich, *Fundamentals of Photonics*, 2nd ed. (Wiley, Hoboken, NJ, 2007).

[81]P. A. Rigg, M. D. Knudson, R. J. Scharff, and R. S. Hixson, "Determining the refractive index of shocked [100] lithium fluoride to the limit of transmissibility," J. Appl. Phys. **116**, 033515 (2014).

[82]J. Pettine, P. Padmanabhan, N. Sirica, R. P. Prasankumar, A. J. Taylor, and H. T. Chen, "Ultrafast terahertz emission from emerging symmetry-broken materials," Light **12**, 133 (2023).

[83]K.-L. Yeh, M. C. Hoffmann, J. Hebling, and K. A. Nelson, "Generation of 10 μJ ultrashort terahertz pulses by optical rectification," Appl. Phys. Lett. **90**, 171121 (2007).

[84]J. Hebling, K.-L. Yeh, M. C. Hoffmann, B. Bartal, and K. A. Nelson, "Generation of high-power terahertz pulses by tilted-pulse-front excitation and their application possibilities," J. Opt. Soc. Am. B **25**, B6–B19 (2008).

[85]H. Hirori, A. Doi, F. Blanchard, and K. Tanaka, "Single-cycle terahertz pulses with amplitudes exceeding 1 MV/cm generated by optical rectification in LiNbO$_3$," Appl. Phys. Lett. **98**, 091106 (2011).

[86]B. K. Ofori-Okai, P. Sivarajah, W. R. Huang, and K. A. Nelson, "THz generation using a reflective stair-step echelon," Opt. Express **24**, 5057–5068 (2016).

[87]M. Savoini, L. Huber, H. Cuppen, E. Abreu, M. Kubli, M. J. Neugebauer, Y. Duan, P. Beaud, J. Xu, T. Rasing, and S. L. Johnson, "THz generation and detection by fluorenone based organic crystals," ACS Photonics **5**, 671–677 (2018).

[88]I. C. Tangen, G. A. Valdivia-Berroeta, L. K. Heki, Z. B. Zaccardi, E. W. Jackson, C. B. Bahr, E. S.-H. Ho, D. J. Michaelis, and J. A. Johnson, "Comprehensive characterization of terahertz generation with the organic crystal BNA," J. Opt. Soc. Am. B **38**, 2780 (2021).

[89]A. Gopal, T. May, S. Herzer, A. Reinhard, S. Minardi, M. Schubert, U. Dillner, B. Pradarutti, J. Polz, T. Gaumnitz, M. C. Kaluza, O. Jäckel, S. Riehemann, W. Ziegler, H. P. Gemuend, and G. G. Paulus, "Observation of energetic terahertz pulses from relativistic solid density plasmas," New J. Phys. **14**, 083012 (2012).

[90]A. Gopal, P. Singh, S. Herzer, A. Reinhard, A. Schmidt, U. Dillner, T. May, H.-G. Meyer, W. Ziegler, and G. G. Paulus, "Characterization of 700 μJ T rays generated during high-power laser solid interaction," Opt. Lett. **38**, 4705–4707 (2013).

[91]A. Gopal, S. Herzer, A. Schmidt, P. Singh, A. Reinhard, W. Ziegler, D. Brömmel, A. Karmakar, P. Gibbon, U. Dillner, T. May, H.-G. Meyer, and G. G. Paulus, "Observation of gigawatt-class THz pulses from a compact laser-driven particle accelerator," Phys. Rev. Lett. **111**, 074802 (2013).

[92]F. Treffert, G. D. Glenn, H. G. Chou, C. Crissman, C. B. Curry, D. P. Deponte, F. Fiuza, N. J. Hartley, B. Ofori-Okai, M. Roth, S. H. Glenzer, and M. Gauthier, "Ambient-temperature liquid jet targets for high-repetition-rate HED discovery science," Phys. Plasmas **29**, 123105 (2022).

09 May 2024 11:47:17